The Astrophysical Journal, 869:71 (9pp), 2018 December 10 https://doi.org/10.3847/1538-4357/aaecd2

Constraining the Volume Density of Dusty Star-forming Galaxies through the First 3 mm Number Counts from ALMA

J. A. Zavala[1], C. M. Casey[1], E. da Cunha[2], J. Spilker[1], J. Staguhn[3,4], J. Hodge[5], and P. M. Drew[1]
[1] The University of Texas at Austin, 2515 Speedway Boulevard Stop C1400, Austin, TX 78712, USA; jzavala@utexas.edu
[2] Research School of Astronomy and Astrophysics, The Australian National University, Canberra ACT 2611, Australia
[3] NASA Goddard Space Flight Center, Code 665, Greenbelt, MD 20771, USA
[4] Bloomberg Center for Physics and Astronomy, Johns Hopkins University 3400 N. Charles Street, Baltimore, MD 21218, USA
[5] Leiden Observatory, Niels Bohrweg 2, 2333 CA Leiden, The Netherlands
Received 2018 August 8; revised 2018 October 23; accepted 2018 October 28; published 2018 December 13

Abstract

We carry out a blind search of 3 mm continuum sources using the ALMA Science Archive to derive the first galaxy number counts at this wavelength. The analyzed data are drawn from observations toward three extragalactic legacy fields: COSMOS, CDF-S, and the UDS comprising more than 130 individual ALMA Band 3 pointings and an effective survey area of ≈200 arcmin^2 with a continuum sensitivity that allows for the direct detection of unlensed Dusty Star-forming Galaxies (DSFGs) dust emission beyond the epoch of reionization. We present a catalog of 16 sources detected at $>5\sigma$ with flux densities $S_{3\,\mathrm{mm}} \approx 60$–$600\ \mu$Jy from which number counts are derived. These number counts are then used to place constraints on the volume density of DSFGs with an empirical backward evolution model. Our measured 3 mm number counts indicate that the contribution of DSFGs to the cosmic star formation rate density at $z \gtrsim 4$ is non-negligible. This is contrary to the generally adopted assumption of a sharply decreasing contribution of obscured galaxies at $z > 4$ as inferred by optical and near-infrared surveys. This work demonstrates the power of ALMA-3 mm observations, which can reach outstanding continuum sensitivities during typical spectral line science programs. Further constraints on 3 mm selected galaxies will be essential to refine models of galaxy formation and evolution as well as models of early universe dust production mechanisms.

Key words: galaxies: general – galaxies: high-redshift – galaxies: star formation – submillimeter: galaxies

1. Introduction

Understanding the star formation activity across cosmic time is among the most important goals of modern observational and theoretical astrophysics. Since around half of optical and UV stellar radiation in galaxies is absorbed by dust and re-emitted at far-infrared (IR) and (sub)millimeter wavelengths, the achievement of a complete unbiased census of the universe's star formation activity requires a multiwavelength approach that reconciles both obscured and unobscured pictures of the universe. While the mapping of cosmic star formation was forged on stellar emission, (sub)millimeter surveys (beginning with Smail et al. 1997; Barger et al. 1998; Hughes et al. 1998) have shown us that the majority of the star formation activity at its peak epoch is primarily enshrouded by dust (Madau & Dickinson 2014). However, while studies of galaxies' rest-frame UV/Optical emission span out to $z \sim 11$ (e.g., Ellis et al. 2013; Oesch et al. 2013; Bouwens et al. 2015; Finkelstein et al. 2015; Finkelstein 2016), our knowledge of the prevalence of dust-obscured star formation at these earlier epochs is completely unconstrained due to the lack of complete samples of $z \gtrsim 4$ dusty star-forming galaxies (DSFGs, see review by Casey et al. 2014).

Though the current large area (sub)millimeter surveys (like those carried out by the *Herschel* Space Observatory and the South Pole Telescope, SPT) have made surprising discoveries of DSFGs up to $z \approx 6$–7 (Riechers et al. 2013; Strandet et al. 2017; Zavala et al. 2018b), they are only sensitive to the rarest, most extreme starbursts with star formation rates (SFRs) of $\gtrsim$1000 $M_\odot$ yr^{-1}, or to gravitationally amplified galaxies whose volume density is difficult to constrain. Less extreme galaxies with SFRs of hundreds of solar masses per year, can in principle be detected in deeper (but smaller area) maps already in-hand from single-dish (sub)millimeter telescopes (e.g., Geach et al. 2017). Nevertheless, the DSFGs identified by these observations (at typical wavelengths of $\lambda = 850\ \mu$m − 1.1 mm) are overwhelmed by the abundant population of $1 < z < 3$ DSFGs (e.g., Michałowski et al. 2017; Zavala et al. 2018a), making the identification of the most distant objects a very challenging task (not to mention the large positional uncertainties of single-dish telescopes). The deep pencil-beam surveys from ALMA (e.g., Umehata et al. 2015; Aravena et al. 2016; Hatsukade et al. 2016, 2018; Walter et al. 2016; Dunlop et al. 2017; Franco et al. 2018) are also dominated by low-redshift sources because of the small survey area and selection wavelength (see the discussion by Casey et al. 2018a). As a consequence, our knowledge of the physical properties and the space density of more moderate luminosity DSFGs with $100 \lesssim \mathrm{SFRs} \lesssim 1000\ M_\odot$ yr^{-1} at high redshifts, and consequently their contribution to the cosmic star formation rate density (CSFRD), is still unknown. Alternative strategies are therefore necessary to characterize the population of DSFGs at the highest redshifts. This is of high importance not only to derive a complete census of the CSFRD but also to shed light on early universe dust production mechanisms and the origin of the universe's first massive galaxies.

The combination of model predictions and integrated measurements such as the number counts, can be used to derive robust constraints on the space density of a population of galaxies (e.g., Béthermin et al. 2012, 2017; Hayward et al. 2013; Cowley et al. 2015), even when individual redshifts of galaxies are not available. Our recently developed empirically motivated backward evolution model of the (sub)millimeter

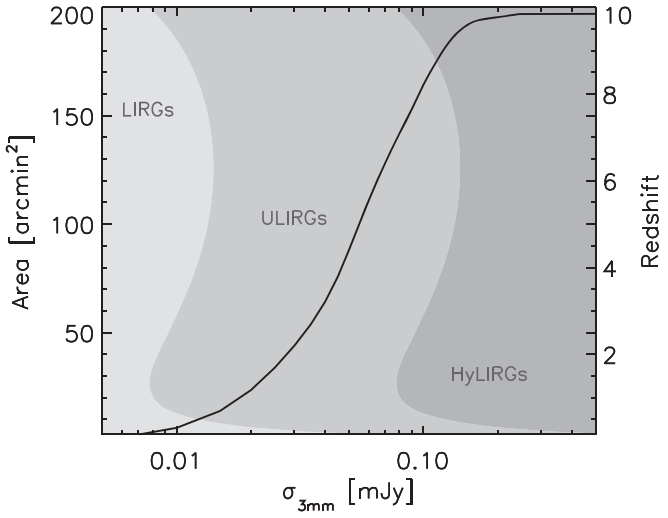

Figure 1. The cumulative area covered by our survey as a function of 1σ rms depth is represented by the black solid line. Additionally, the corresponding luminosity detection limit at 5σ is shown as a function of redshift assuming a typical DSFG SED (a graybody with $T_D = 35$ K and $\beta = 1.8$), including the impact of CMB (da Cunha et al. 2013). Three luminosity ranges are illustrated: LIRGs ($10^{11} \leqslant L_{\rm IR} < 10^{12}\,L_\odot$), ULIRGs ($10^{12} \leqslant L_{\rm IR} < 10^{13}\,L_\odot$), and HyLIRGs ($L_{\rm IR} \geqslant 10^{13}\,L_\odot$). Given the strong negative K-correction in the 3 mm band, we are sensitive to galaxies with $L_{\rm IR} \gtrsim 10^{12}$–$10^{13}\,L_\odot$ up to $z \sim 10$.

sky (Casey et al. 2018a, 2018b) adopts an evolving infrared galaxy luminosity function (IRLF) between $0 < z \lesssim 10$ to make predictions, as a function of (sub)millimeter wavelength and depth, of the number counts and redshift distribution of galaxies selected in the far-infrared (FIR) and (sub)millimeter regime. As thoroughly discussed in Casey et al. (2018a, 2018b), the constraints provided by all the current submillimeter and millimeter surveys from both single-dish and interferometric observations are not tight enough to draw strong conclusions on the shape of the IRLF (and hence on the contribution of these galaxies to the CSFRD) at $z > 2.5$. This lack of constraining power is illustrated by the fact that the aggregate of two decades of data at (sub)millimeter wavelengths cannot distinguish between two extreme hypothetical scenarios: a dust-rich universe where the CSFRD at $z > 4$ is dominated ($\gtrsim$90%) by DSFGs and an alternate dust-poor early universe where dust-obscured star formation at $z > 4$ is negligible (see Casey et al. 2018a, 2018b). An important corollary of these studies suggests that surveys at longer wavelengths than those carried out in the past, specifically observations at 2 mm (e.g., Staguhn et al. 2014) and 3 mm, represent a promising way to identify and characterize the high-redshift population of DSFGs by effectively filtering out low-redshift sources.

This work represents one of the first efforts to exploit 3 mm continuum observations for the detection of such distant objects. Selection at 3 mm is an extension of the submillimeter-galaxy selection technique to the extreme. Indeed, galaxies found at 3 mm are unlikely to lie at $z < 2$ due to the very strong millimeter negative K-correction (Figure 1, see also Casey et al. 2018a). Though the detection of these galaxies requires very deep observations (since 3 mm flux density arises from the faint tail of the Rayleigh–Jeans regime of the dust thermal emission), this depth is routinely achieved in ALMA spectroscopic surveys upon collapsing data cubes across the spectral dimension. Indeed, five 3 mm selected continuum sources have already been reported in the recent literature: one in the ASPECS-Pilot survey with a redshift of 2.543 (Aravena et al. 2016; Walter et al. 2016) and four revealed conducting a spectral program analyzing source multiplicity in DSFGs (Wardlow et al. 2018). Here we report the results of a blind search for 3 mm detected sources, as discussed in Section 2, and the first estimation of the 3 mm galaxy number counts derived from ALMA observations, which is presented in Section 3. These sources were found in ALMA archival data sets covering a total solid angle of 198 arcmin^2 in three different extragalactic survey fields: UDS, CDF-S, and COSMOS. The constraints provided by the number counts on the IRLF are described in Section 4 as well as the estimated dust-obscured SFR density. Finally, our conclusions are presented in Section 5.

We assume a Planck cosmology throughout this paper, adopting $H_0 = 67.7$ km s^{-1} Mpc^{-1} and $\Omega_\Lambda = 0.69$ (Planck Collaboration et al. 2016), and the Chabrier (2003) initial mass function (IMF) for SFR estimations.

2. Data Retrieval, Analysis, and Characterization

Galaxies' 3 mm dust continuum emission is expected to be several times fainter than their flux densities measured at shorter wavelengths (like the standard (sub)millimeter wavebands at $\lambda \approx 850$–$1100\,\mu$m) due to the shape of the dust spectral energy distribution (SED) on the Rayleigh–Jeans tail. For example, a typical galaxy in the Casey et al. (2018a, 2018b) simulations at $z \sim 2$ has a flux ratio of $S_{1.2\rm mm}/S_{3\rm\,mm} \sim 25$, or a flux ratio of $S_{1.2\rm mm}/S_{3\rm\,mm} \sim 10$ at $z \sim 5$. For this reason, 3 mm observations are not an efficient method for detecting dust continuum emitters blindly, and therefore, no 3 mm continuum-only blank field exists to date. However, most of the spectroscopic studies of molecular gas in low and high-redshift galaxies are conducted in this waveband due to the large coverage of ^{12}CO transitions (see, for example, Figure 1 from Walter et al. 2016). Since these spectral observations require deep sensitivity across relatively narrow frequency channels (with a velocity resolution on the order of $\approx$10–100 km s^{-1}), the typical achieved continuum depth across the total 8 GHz bandwidth, in the case of ALMA, is enough to detect galaxies' dust emission up to very high redshifts, as shown in Figure 1. This work exploits ALMA archival Band 3 data to perfom a blind search of 3 mm continuum-detected galaxies to derive the first number counts and to constrain the volume density of DSFGs.

2.1. ALMA Band 3 Archival Data

Using the ALMA Science Archive Query, we search for public ALMA Band 3 observations, which cover a frequency range of $\nu = 84$–116 GHz or $\lambda = 2.59$–3.57 mm. We focused only on data acquired from Cycle 3 onward, when the ALMA Science Pipeline was already commissioned, and continuum maps were also processed and available through the archive. To avoid contamination from Galactic sources, the search was limited to programs carried out within three well-known cosmological fields: UDS, CDF-S, and COSMOS, which comprise the vast majority of extragalactic Band 3 science pointings. Furthermore, these fields have exquisite ancillary multiwavelength data that allows a detailed characterization of the detected 3 mm sources (e.g., Laigle et al. 2016). A restriction on the angular resolution of the images, $\theta \geqslant 1.0$ arcsec, was also imposed in order to avoid the incompleteness

Table 1
3 mm ALMA Archival Survey Source Catalog

ID	R.A. (hh:mm:ss.s)	Decl. (°:′:″)	S/N	$S_{3\,\mathrm{mm}}$[a] (μ Jy)	z_{spec}	Other Names
ALMA-3 mm.01[b]	03:31:09.8	−27:52:25.6	24.0	240 ± 10	⋯	ALESS 41.C[c]
ALMA-3 mm.02	02:16:44.3	−05:02:59.7	8.7	118 ± 14	⋯	⋯
ALMA-3 mm.03	03:32:38.6	−27:46:34.5	8.5	57 ± 7	2.54[d]	ASPECS-3 mm.1[d]
ALMA-3 mm.04	02:17:42.8	−03:45:31.2	7.4	130 ± 18	⋯	⋯
ALMA-3 mm.05[e]	10:01:30.7	+02:18:41.4	6.8	129 ± 19	⋯	⋯
ALMA-3 mm.06	03:31:02.9	−28:42:29.8	6.7	117 ± 17	⋯	⋯
ALMA-3 mm.07	03:31:26.7	−27:56:01.0	6.6	53 ± 8	⋯	ALESS 75.C[c]
ALMA-3 mm.08	10:00:54.5	+02:34:36.2	6.2	164 ± 26	4.55[f]	AzTEC-C17[g]
ALMA-3 mm.09	03:32:50.7	−27:31:34.7	6.1	63 ± 10	⋯	ALESS 87.C[c]
ALMA-3 mm.10	02:16:44.5	−05:02:21.6	5.9	91 ± 16	⋯	S2CLS-UDS.0074,[h] ASXDF1100.003.1[i]
ALMA-3 mm.11[e]	10:00:33.3	+02:26:01.2	5.4	126 ± 23	2.51[j]	AzTEC-C80b[k]
ALMA-3 mm.12	10:00:34.4	+02:21:21.7	5.4	125 ± 23	2.99[j]	⋯
ALMA-3 mm.13	03:30:56.0	−28:43:04.1	5.3	104 ± 19	⋯	⋯
ALMA-3 mm.14	03:32:49.5	−27:32:07.6	5.2	98 ± 19	⋯	⋯
ALMA-3 mm.15	10:00:22.4	+02:31:38.7	5.2	610 ± 120	⋯	⋯
ALMA-3 mm.16	10:02:00.1	+02:24:18.1	5.0	263 ± 52	⋯	⋯

Notes.
[a] Measured flux density scaled to 3 mm (see Footnote 6).
[b] This source was not included in the number counts due to the nonthermal emission (see Section 2.2).
[c] Wardlow et al. (2018).
[d] Walter et al. (2016).
[e] This source was not included in the number counts since it may be physically associated with the primary target of the observations.
[f] Schinnerer et al. (2008).
[g] Aretxaga et al. (2011).
[h] ALMA project code: 2015.1.01528.S.
[i] Ikarashi et al. (2017).
[j] J. Zavala et al. (2018, in preparation).
[k] Brisbin et al. (2017).

effects associated with high angular resolutions (see Franco et al. 2018) and to avoid resolving out the emission of the galaxies. Finally, observations were restricted to have a continuum sensitivity of $\sigma_{\mathrm{rms}} < 0.2$ mJy beam^{-1}, which roughly corresponds to the minimum depth required for the detection of unlensed DSFGs with SFRs $\lesssim 1000\,M_{\odot}$ yr^{-1} (see Figure 1).

After removing spatially overlapping observations and projects with no continuum images available, a total of 135 maps were retrieved from almost 20 different projects (up to a public release date of 2018 May), including not only single pointings but also mosaics made of several pointings (all ALMA project codes are reported in the Acknowledgments). This compilation covers an effective area of 198 arcmin^2, equivalent to the area encompassed by ∼240 ALMA Band 3 pointings within the primary beam FWHM ($\theta_{\mathrm{FWHM}} \approx 60''$). This is an order of magnitude larger than the typical contiguous blank fields achieved with this facility (e.g., Umehata et al. 2015; Hatsukade et al. 2016, 2018; Walter et al. 2016; Dunlop et al. 2017). Figure 1 shows the total area analyzed in this work as a function of depth.[6]

The primary science goal of most of these projects was to detect spectroscopic features, particularly CO emission lines, in targets selected from heterogeneous criteria (e.g., optically selected galaxies, blank fields, proto-cluster, and cluster environments, etc.). This sample selection does not introduce any obvious bias in our blind search, since we are targeting continuum-selected galaxies that are expected to be high-redshift ($z > 2$) DSFGs (see Section 2.2 and the Appendix). In fact, as revealed by a quick visual inspection, only a few of the original targets are detected in the continuum images. These sources are not included in our source catalog.

Since continuum observations are not the primary science goal of the original projects, a further test on the quality of the retrieved continuum images was conducted. For maps where continuum sources were detected (see Section 2.2), we individually re-reduce the raw data using CASA (McMullin et al. 2007) following the standard procedure, with a natural weighting of the visibilites in order to maximize the sensitivity to faint sources. The measured flux densities of the detected sources (see Table 1) are in very good agreement with the values measured on the maps available through the archive—although the signal-to-noise ratio (S/N) is typically lower in the retrieved images since a Briggs weighting is usually adopted.

2.2. Source Extraction and Source Catalog

Source extraction was performed using the uncorrected primary beam continuum maps (which have the benefit of a constant noise) within a radius of ≈1.3 times the FWHM of the primary beam, where the antenna response sensitivity is ⩾0.3. A central square mask with a side's dimension of 2 times the size of the synthesized beam is also applied on the primary target of each program.

[6] The quoted depth of the observations and the flux densities of the detected sources have been scaled to 3 mm (99.9 GHz, the central frequency of Band 3) assuming $S_{\nu} \propto \nu^{2+\beta}$, with $\beta = 1.8$ (a modified Rayleigh–Jeans law). This correction is usually of the same order (or less) than the typical flux boosting factor and/or the typical flux uncertainty.

To search for source candidates, the uncorrected primary beam map of each observation is first divided by the noise of the same image to obtain a signal-to-noise map. The noise is assumed to be the 68th percentile of the distribution of pixel values of the map, which corresponds to 1σ for a Gaussian distribution.[7] The 68th percentile is preferred over the standard deviation of the map since the latter can be overestimated by the presence of real sources. Then, source candidates are identified by searching pixels above a signal-to-noise threshold, and the associated flux density of each candidate is measured from the primary beam corrected image at the same position and its error is assumed to be the noise measured in the whole uncorrected primary beam map divided by the primary beam response at the same pixel. Although values of S/N ≈ 3–4 have been used in the literature (e.g., Hodge et al. 2013; Fujimoto et al. 2016), the large number of independent beams in ALMA maps, compared to single-dish observations, produces a significant contamination rate at these low S/Ns (Dunlop et al. 2017). Thus, here we adopt a conservative threshold of 5σ to minimize the contamination fraction (see Section 2.3). Finally, a mask of 2 times the FWHM of the synthesized beam is applied at the position of the source candidate before repeating the process again until no more $>5\sigma$ pixels are found.

The 16 serendipitously detected 3 mm sources at $>5\sigma$ are reported in Table 1 along with the their individual S/Ns, flux densities, and their associated uncertainties. This catalog includes the previously detected source in the ASPECS survey (Walter et al. 2016) and three of the sources found in Wardlow et al. (2018). The remaining detection reported by Wardlow et al. ALESS 49.C, falls just below our adopted threshold and hence is not included in the catalog.

A thorough investigation of the potential contaminants is important to ensure the purity of the catalog. As discussed by Wardlow et al. (2018), it is possible that sources' 3 mm emission arises from nonthermal processes. Actually, ALMA −3 mm.01 (also known as ALESS 41.C) shows an SED consistent with a flat-spectrum radio quasar and might be associated with a known radio source. This object has therefore not been included in the number counts estimation described below. To rule out the possibility of including any other source with a nonthermal SED we re-reduce the ALMA data and create two continuum maps for each source with the spectral windows corresponding to the low and high frequency sidebands, respectively. All of the sources show properties consistent with thermal emission (i.e., $S_{\nu_{\rm high}}/S_{\nu_{\rm low}} > 1$), with possible exceptions of ALMA-3 mm.15 and ALMA-3 mm.16, for which the low S/Ns on the individual (split) continuum maps prevent a robust determination; their colors might be consistent with a flat-spectrum (although at low $\lesssim 3\sigma$ significance). A further analysis of the extracted spectrum for these objects revealed that sources ALMA-3 mm.05 and ALMA-3 mm.11 may be physically associated with, or at the same redshifts as, the original targets of their observations, based on the presence of millimeter emission lines at similar frequencies (J. Zavala et al. 2018, in preparation). These two sources are hence not considered in the number counts estimation aimed at reporting an unbiased statistic, but are reported in the catalog given the adopted selection criterion. A deeper analysis of the nature of these sources as well as a full characterization of their physical properties require a multi-wavelength analysis, which will follow in a future paper. In the meantime, a brief description of the 13 sources used in the number counts analysis is presented in the Appendix, emphasizing the potential biases introduced by the original targets of these observations that might affect the *blindness* of this survey.

[7] The noise distribution of ALMA observations has been shown to be well described by Gaussian noise, especially in the case of unresolved or marginally resolved faint sources; e.g., Dunlop et al. (2017).

2.3. Completeness, Flux Boosting, and Contamination

The measurement of the number counts requires an estimate of the completeness of the survey, the contamination rate, and the magnitude of the flux boosting, an effect that systematically increases the measured flux densities of sources detected at relatively low S/Ns.

To estimate the contamination from false detections, we repeat the source extraction procedure described above after inverting all of the 3 mm continuum maps. All the peaks present in these inverted maps are expected to be noise fluctuations. The spurious fraction is then estimated as the ratio of the number of negative-to-positive peaks as a function of S/N, where the errors are estimated through a bootstrapping method. As shown in Figure 2, a false detection rate of $\lesssim$5% is expected at our adopted threshold of $\geqslant 5\sigma$. This is in agreement with the results of previous ALMA studies, which determined that the rate of false detections falls close to zero at this S/N threshold (e.g., Simpson et al. 2015; Fujimoto et al. 2016; Oteo et al. 2016).

The completeness and flux boosting were quantified using Monte Carlo simulations. Artificial sources are first injected into the flux maps and then they are recovered with the same source extraction procedure used to build the real source catalog. A source is considered recovered if it is detected within a synthesized beam of the input random position. After 100 realizations per S/N bin, ranging from 3.0 to 7.0 in steps of 0.1, we determine a completeness of $\gtrsim$70% at S/N $\geqslant$ 5.0, increasing up to $\gtrsim$95% at S/N $\gtrsim$ 6.0 (Figure 2). The average flux boosting factor due to Eddington bias, measured as the ratio of output-to-input flux density, is found to be ∼10% at 5.0σ, with the boost factor falling to $\lesssim$5% at $\gtrsim 6.0\sigma$. Uncertainties in both completeness and flux boosting are estimated as the standard deviation in each bin of S/N and are then propagated in the estimation of the number counts (see Section 3).

3. Number Counts

Though no ALMA-3 mm number counts exist in the literature so far, galaxy number counts have been well studied at shorter wavelengths ($\lambda = 850\,\mu$m − 1.3.mm) using blind ALMA observations (e.g., Hatsukade et al. 2013, 2018; Carniani et al. 2015; Fujimoto et al. 2016; Oteo et al. 2016; Franco et al. 2018). In this paper, we follow the typical method used previously in those works. The contribution of a source with a deboosted flux sensity, S_i, to the cumulative number counts are estimated to be:

$$N_i(S_i) = \frac{1 - f_{\rm cont}}{\zeta\, A_{\rm eff}(S_i)}, \quad (1)$$

where $f_{\rm cont}$ is the estimated fraction of contamination at the measured S/N of the source, ζ is the corresponding completeness, and $A_{\rm eff}(S_i)$ is the largest integrated area sensitive enough

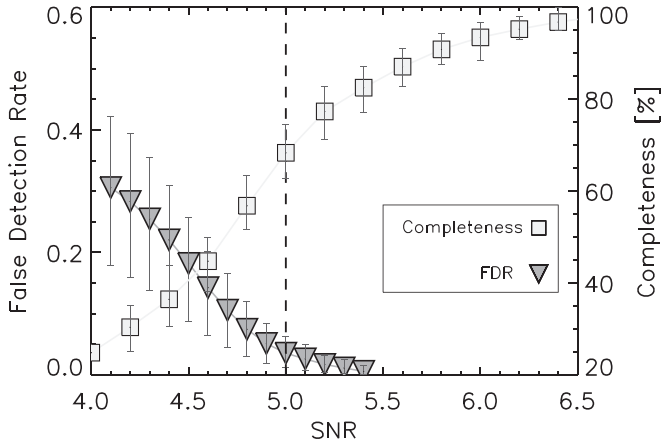

Figure 2. Estimated contamination from spurious sources (dark gray triangles) and completeness (light gray squares) and as a function of S/N of the detected sources. The 5σ adopted threshold is represented by the dashed vertical line, where the false detection rate and completeness are expected to be $\lesssim$5% and $\gtrsim$70%, respectively.

to detect sources with $S \geqslant S_i$ at our adopted threshold (see Figure 1). As mentioned in Section 2.3, a low contamination rate ($\lesssim$5%) is expected given our conservative selection criterion, while the completeness of the survey is found to be $\approx$70%–100% (see Figure 2). Finally, the cumulative number counts, $N(>S)$, is estimated by the sum over all of the sources with a flux density higher than S.

To derive reliable uncertainties in our estimation of the number counts, we take into account the errors associated to the flux densities and survey's completeness through a Monte Carlo simulation, where random values are extracted in each realization from Gaussian distributions with standard deviations equal to the measured errors. Given our small sample size of 13 sources, Poisson uncertainties are also added in quadrature following Gehrels (1986), which are indeed the dominant contributors. Figure 3 shows our final cumulative number counts as a function of flux density and the associated uncertainties, after removing the three sources noted in Section 2.2 (thought to be either nonthermal or associated with the original targets). These estimations are likely to be low biased by cosmic variance since observations across different sightlines were analyzed.

To parameterize the number counts we fit a double-power law of the form

$$N(>S) = N_0\left[\left(\frac{S}{S_0}\right)^{\alpha} + \left(\frac{S}{S_0}\right)^{\beta}\right]^{-1}, \quad (2)$$

where N_0, S_0, α, and β describe the normalization, break, and slope of the power laws, respectively. The best-fit parameters, $N_0 = 1200^{+1400}_{-1100}$, $S_0 = 0.11^{+0.22}_{-0.03}$ mJy, $\alpha = 1.4 \pm 0.5$, and $\beta = 3.4 \pm 0.5$, were inferred using a minimum χ^2 method through a Levenberg–Marquardt algorithm. The resultant best-fit double-power law is plotted in Figure 3. The number counts were also fitted with a Schechter-like function, but it reproduce neither the behavior of the data at the brightest flux densities nor the shape of the number counts at the faintest end.

The estimated number counts imply that one serendipitous DSFG is detected at 5σ per three ALMA Band 3 continuum maps with one hour of integration. This calculation assumes a search area equal to 1.3 times the FWHM of the primary beam

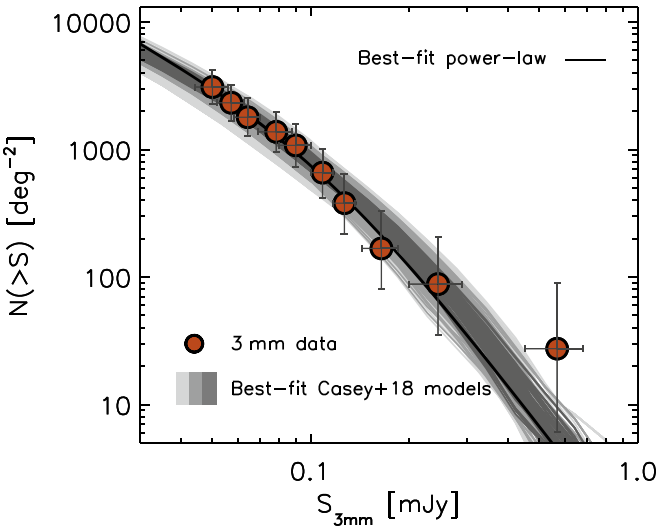

Figure 3. Integral galaxy number counts at 3 mm. The measurements derived in this work are represented by the red points and the best-fit broken power is plotted as the black solid line. We also plot the number counts from the Casey et al. (2018a, 2018b) model when different evolutions on the IRLF are assumed, which are used to fit the data through a maximum likelihood estimation method. The 68%, 95%, and 99.7% confidence intervals for the best-fit models are color-coded from the darkest to the lightest gray, respectively. Their corresponding contributions to the cosmic star formation rate density are plotted in Figure 5.

($\approx$1.3 arcmin^2) and a depth equal to $\sigma \approx 20$ μJy beam^{-1}. This implies that an even more significant sample of 3 mm detected sources can be built using only ALMA archival observations over the next few years. Similarly, these sources might be detected in the deepest maps achieved at this wavelength with the MUSTANG2 camera on the Green Bank Telescope (e.g., T. Mroczkowski et al. 2018, in preparation), albeit with low angular resolution and higher integration times compared with ALMA.

4. Constraining the IRLF

In this section we use the estimated galaxy number counts and the predictions from the backward evolution model presented by Casey et al. (2018a, 2018b) to constrain the IRLF, and thus, the contribution of DSFGs to the CSFRD. The model first adopts an IRLF of the form

$$\Phi(L, z) = \begin{cases} \Phi_\star(z)\left(\dfrac{L}{L_\star(z)}\right)^{\alpha_{\rm LF}(z)}, & \text{if } L < L_\star, \\ \Phi_\star(z)\left(\dfrac{L}{L_\star(z)}\right)^{\beta_{\rm LF}(z)}, & \text{if } L \geqslant L_\star, \end{cases} \quad (3)$$

and assumes an evolution between $0 < z \lesssim 10$. At $z \lesssim 2$, the evolution is well constrained by direct measurements of the IRLF from single-dish telescope data sets; however, at higher redshifts different evolutions are explored. Each galaxy extracted from the assumed IRLF is then assigned an SED according to its luminosity and redshift, following the luminosity-dust temperature (or $L_{\rm IR} - \lambda_{\rm peak}$) relation and correcting for CMB effects (da Cunha et al. 2013). Finally, mock observations of the sky are obtained at different wavelengths, areas, and depths, which are used to generate mock measurements of number counts and redshift distributions.

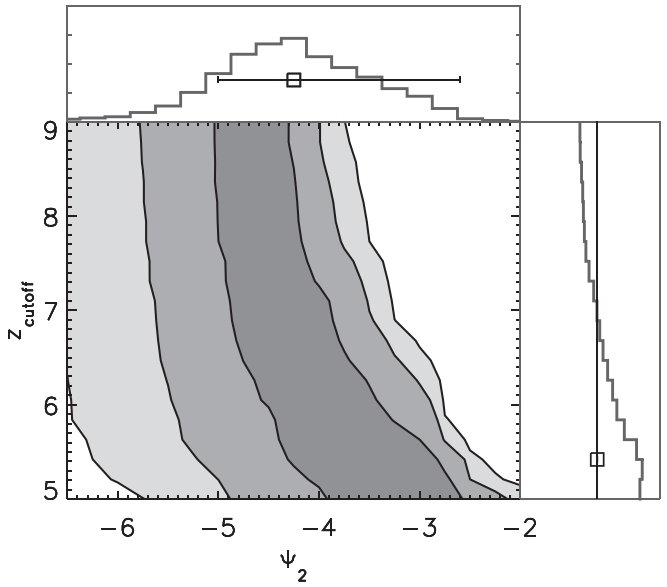

Figure 4. 68%, 95%, and 99.7% confidence intervals (represented by the contours in the gray-scale image) for the two parameters explored in this work to describe the evolution of the IRLF in the Casey et al. (2018a, 2018b) models. The confidence intervals were determined by fitting the corresponding predicted number counts through a maximum likelihood approach. The derived probability distribution for each individual parameter is represented by the solid line in the external panels (top and right, respectively).

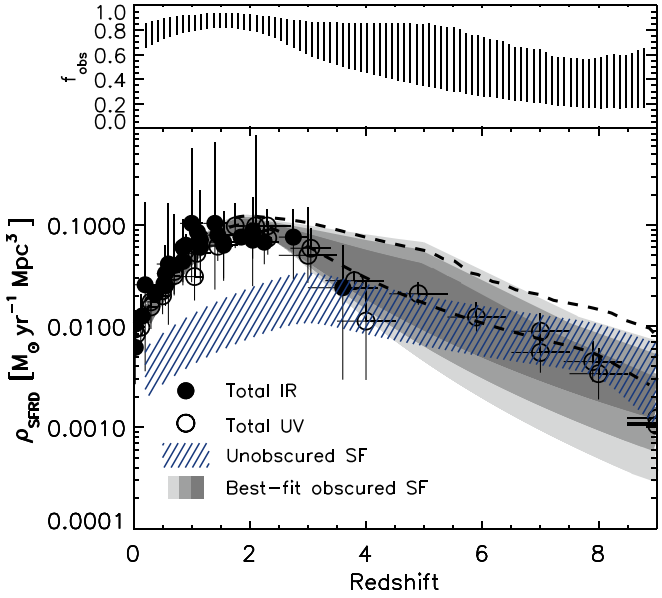

Figure 5. Cosmic star formation rate density as a function of redshift, comparing measurements from rest-frame UV/optical to the obscured component constrained by our 3 mm number counts. Black circles represent measurements from the literature from both dust-corrected UV (empty circles) and IR rest-frame (filled circles) studies (Madau & Dickinson 2014), which are dominated by UV surveys at $z \gtrsim 3.5$. The implied star formation rate densities of the Casey et al. (2018a, 2018b) models that best fit the measured 3 mm number counts are illustrated by the gray regions, where the darkest gray represents the 68% confidence interval (the 95% and 99.7% are plotted with lighter grays, respectively). On the other hand, the unobscured sources' contribution derived from UV-based measurements, uncorrected by dust attenuation, is represented by the blue hashed region. The implied total (obscured + unobscured) CSFR is represented by the region delimited by the dashed black lines (68% confidence interval). Finally, the fraction of obscured star formation (SF_{IR}/SF_{UV+IR}) as a function of redshift derived from the best-fit model predictions is shown in the top panel.

The reader is referred to Casey et al. (2018a, 2018b) for a thorough description of the model and how sources' flux densities map to the modeled IRLF.

The characteristic number density of the luminosity function, $\Phi_\star$, is assumed to evolve as $(1+z)^{\psi_1}$ with a redshift turnover, $z_{\rm turn} \approx 2$, from which the relation evolves at higher redshifts with a different slope, ψ_2, so that:

$$\Phi_\star \propto \begin{cases} (1+z)^{\psi_1}, & \text{if } z < z_{\rm turn}, \\ (1+z)^{\psi_2}, & \text{if } z > z_{\rm turn}. \end{cases} \quad (4)$$

As discussed in the works by Casey et al. the parameters ψ_1 and $z_{\rm turn}$ are fixed to reproduce direct measurements of the luminosity function and the CSFRD at $z \lesssim 2.5$, while ψ_2 is unconstrained. In this work, we explore different values for this parameter ranging from $\psi_2 = -6.5$ to -2.0, which map to a very dust-poor early universe and to an extremely dust-rich one, respectively. Additionally, an extra parameter, $z_{\rm cutoff}$, is used in this analysis to define a redshift above which no more dust-rich galaxies exist, ranging from $z_{\rm cutoff} = 9$ down to 5. The different evolutionary models of the IRLF are combined with the modeled SEDs to create mock observations from which the number counts are derived. The simulated number counts are then used to fit the measurements derived in Section 3 through a maximum likelihood approach, using flat prior distributions for both ψ_2 and $z_{\rm cutoff}$. The corresponding 3 mm number counts from these models are shown in Figure 3, where the best-fit 1, 2, and 3σ confidence intervals are illustrated by the different colors.

As shown in Figure 4, the best-fit values measured from the 3 mm number counts provide weak constraints on $z_{\rm cutoff}$ but stronger constraints on Ψ_2 with a best-fit value of $\Psi_2 = -4.2^{+1.6}_{-0.8}$. Though the range of consistent models is large, indicating significant uncertainty in the yet small 3 mm sample, we highlight that a dust-poor universe where DSFGs contribute negligibly (<10%) to the CSFR at $z > 4$ ($\psi_2 < -5.3$) is not favored by the data. And yet such a sharp downward evolution in the IRLF is widely assumed in the literature (e.g., Bouwens et al. 2015; Finkelstein et al. 2015). Actually, as shown in Figure 5, the best-fit models predict that DSFGs contribute ≈35%–85% of the total CSFRD at $z \approx 4$–5 (68% confidence interval). This implies that the current measurements of the total CSFR at high redshifts, which are based mostly on UV/optical studies of Lyman Break Galaxies samples, might be underestimated up to a factor of ∼5. At higher redshifts ($z > 5$), due the degeneracy between $z_{\rm cutoff}$ and ψ_2 (see Figure 4), two scenarios can be constrained. A low $z_{\rm cutoff}$ value of ≈6 implies that the contribution from DSFGs to the CSFRD is indeed negligible at $z \gtrsim 6$, but as high as the current measurements derived from surveys tracing the unobscured star formation at $z \lesssim 6$. In other words, DSFGs contribute up to ≈75% of the total SFR density up to $z \sim 6$. Beyond this redshift, the total CSFRD would be represented by the current measurements obtained from UV/Optical surveys. On the other hand, if DSFGs are allowed to exist in the model up to $z_{\rm cutoff} \sim 9$, the contribution per redshift bin is non-negligible even at $z \sim 9$ (although with a large range of uncertainty of ≈15%–65%). This later scenario would imply that the current measurements of the total CSFRD are thus biased even at the highest redshifts.

A further analysis of the assumed dust optical depth is important to understand any possible bias in these estimations.

Although, in the model, the SEDs are parameterized as a function of $\lambda_{\rm peak}$ instead of dust temperature, the impact of the CMB on the heating and detection of these sources is a strong function of the dust temperature, and hence, the choice of the dust opacity introduces some differences on the galaxies' detected flux densities at the highest redshifts. The constraints described above assume optically thick SEDs at rest-frame $\lambda < 100$ μm due to the dust self-absorption often present in highly obscured systems. This scenario is supported by the high dust mass typically measured for these galaxies (e.g., Michałowski et al. 2010; Magdis et al. 2012). However, if an optically thin SED is adopted in the model, the number density of galaxies required to reproduce the same number counts is higher, given the stronger effect of the CMB due to the lower dust temperatures associated to the optically thin assumption. Consequently, the universe would need to be more dust-rich than the one predicted by the optically thick assumption discussed above.

Tighter constraints on the obscured CSFRD can be obtained from the redshift distribution of these sources, which can be directly compared to the predictions from the model. Actually, the best-fit models predict that ≈80%–90% of the sources with $S_{3\,\rm mm} > 50$ μJy (as those reported here) lie at $z > 2$ and ≈15%–35% at $z > 4$ (68% confidence interval). The high-redshift tail of the expected redshift distribution is then more significant than the ones measured for galaxies selected at shorter wavelengths. For example, Danielson et al. (2017) found that only ∼10% of the galaxies selected at 870 μm are at $z > 4$. However, only four of the sources in our catalog have spectroscopic redshifts (see Table 1) and, although very low-redshift solutions can be discarded, the current ancillary data is not enough to derive precise photometric redshifts for all the sources since some of them lie outside of the deep imaging surveys. The analysis of the redshift distribution of these galaxies will hence be presented in a subsequent work along with recently accepted follow-up ALMA Cycle 6 observations (PI: J. Zavala).

5. Conclusions

We have exploited the ALMA archive to conduct a blind search of serendipitously detected 3 mm continuum sources, an extension of the submillimeter-galaxy selection technique to detect DSFGs at high redshifts. The analyzed data cover a total area of ≈200 arcmin^2, which is equivalent to the area of ≈240 ALMA primary beams in this band, an order of magnitude larger than the areas mapped to date in blank-field contiguous observations with ALMA. After masking out the observations' primary targets, we have detected 16 sources above the adopted conservative threshold of 5σ, at which the expected false detection rate is <5%. Using these sources we have derived the first number counts at 3 mm and estimated that one source is expected per three ALMA Band 3 maps for one hour of integration.

Using the predictions of a backward evolution model, we have found that a dust-poor universe where DSFGs contribute negligibly to the CSFR at $z > 4$, as commonly adopted in the literature, is not favored by the data. The best-fit models for the evolving IRLF predict that DSFGs contribute ≈35%–85% of the total CSFRD across $z \approx 4$–5. At higher redshifts the contribution from dust-obscured star formation is less constrained due to the degeneracy between parameters in the model. The limits of our constraints themselves could be represented by two broadly different scenarios: a high obscured contribution up to ≈75% to the total CSFRD up to $z \sim 6$, above which the obscured star formation is much more rare, or a non-negligible but more uncertain contribution (≈15%–65%) up to $z \sim 9$. Since these dust-obscured galaxies are not included in the UV/Optical studies, from which most of the measurements of the CSFRD at high-redshift have been derived, this work suggests that our current understanding of the CSFRD at $z > 4$ is still incomplete.

This work highlights the power of 3 mm observations to detect DSFGs and to measure the dust-obscured SFR density at the earliest epochs, even when spectroscopic redshifts for individual sources are not available. Given the practice of carrying out millimeter spectral line surveys at this wavelength, a large number of serendipitous detections of 3 mm continuum sources are expected during the next few years, from which more robust constraints on the dust-obscured SFR density can be derived as well as on early universe dust production mechanisms and galaxy formation and evolution models.

This work would not have been possible without the rich data available through the ALMA Science Archive.

We thank the reviewer for a helpful report that improved the clarity of the paper. J.A.Z. and C.M.C. thank the University of Texas at Austin College of Natural Sciences for support. We also thank NSF grants AST-1714528 and 1814034. E.d.C. gratefully acknowledges the Australian Research Council for funding support as the recipient of a Future Fellowship (FT150100079).

This paper makes use of the following ALMA data: ADS/JAO.ALMA#2013.1.00092.S, ADS/JAO.ALMA #2015.1.00853.S, ADS/JAO.ALMA#2016.1.00171.S, ADS/JAO.ALMA#2016.1.00567.S, ADS/JAO.ALMA #2016.1.00932.S, ADS/JAO.ALMA#2015.1.00228.S, ADS/JAO.ALMA#2015.1.01151.S, ADS/JAO.ALMA #2016.1.00324.L, ADS/JAO.ALMA#2016.1.00754.S, ADS/JAO.ALMA#2016.1.00967.S, ADS/JAO.ALMA #2015.1.00752.S, ADS/JAO.ALMA#2015.1.00862.S, ADS/JAO.ALMA#2015.1.01222.S, ADS/JAO.ALMA #2016.1.00698.S, ADS/JAO.ALMA#2016.1.00798.S, ADS/JAO.ALMA#2016.1.01546.S, ADS/JAO.ALMA #2016.1.00564.S, ADS/JAO.ALMA#2016.1.01149.S. ALMA is a partnership of ESO (representing its member states), NSF (USA) and NINS (Japan), together with NRC (Canada) and NSC and ASIAA (Taiwan) and KASI (Republic of Korea), in cooperation with the Republic of Chile. The Joint ALMA Observatory is operated by ESO, AUI/NRAO and NAOJ.

Facility: ALMA.

Appendix
On the Possible Selection Biases

While some of the archival observations used in this work are actually unbiased blank-field observations, the original targets of some other projects might introduce some biases on the estimated space density of the 3 mm selected galaxies, particularly if the sources targeted are associated with over-dense regions, are known to have a strong clustering, or exhibit a high source multiplicity. In this section, we investigate the selection biases of each of the 13 sources used in the number counts estimation and conclude that our estimations are not significantly biased.

ALMA-3 mm.02, ALMA-3 mm.10: Both sources were found in the same ALMA observations (#2015.1.00862.S), which

target the CO(3 − 2) transition in a $z = 2.24$ galaxy selected from wide and deep narrowband H_α surveys (R.A. = 02:16:45.8, decl. = −05:02:44.7; Sobral et al. 2013; Molina et al. 2017). The original source is not detected in the ALMA continuum image, from which we derive a flux density upper limit of $S_{3\,\mathrm{mm}} < 21$ mJy (3σ). This a factor of 6 and 3 fainter than our 3 mm candidates ALMA-3 mm.02 and ALMA-3 mm.10, which are located at 31 and 28 arcsec from the main target, respectively. All this information suggests that our source candidates are not related to the original one. Actually, ALMA-3 mm.10 is part of an independent ALMA follow-up of AzTEC sources at 1.1 mm (Ikarashi et al. 2017), and despite having a similar flux density to other sources in the catalog whose redshift distribution peaks between $z = 2$–3, it lacks a photometric redshift estimation, suggesting a higher redshift solution.

ALMA-3 mm.03: This source was found in the observations of the ASPECS project (ALMA project code: #2016.1.00324; see also Walter et al. 2016), which by design is an ubiased blank-field survey.

ALMA-3 mm.04: The source was detected in the ALMA program #2016.1.00698.S, which aims to detect the Sunyaev–Zeldovich effect in a galaxy cluster at $z = 1.91^{+0.19}_{-0.21}$ (Mantz et al. 2014). A further analysis of the extracted spectrum of this candidate revealed a line at 105.27 GHz (J. Zavala et al. 2018, in preparation), which is inconsistent with the cluster redshift (the closest solution to the cluster's redshift is $z = 2.28$). Therefore, this indicates that our galaxy is not associated with the cluster structure.

ALMA-3 mm.06, ALMA-3 mm.13: The ALMA observations (#2015.1.01151.S) target the CO(2−1) transition in galaxies within a proto-cluster at $z = 1.6$. Despite being detected in the continuum maps, our detections do not show any features at ∼88.2 GHz, the expected frequency for the CO(2−1) line given the proto-cluster redshift. Indeed, one of our sources (ALMA-3 mm.13), shows a line at ∼99.8 GHz (J. Zavala et al. 2018, in preparation), which confirms that the source is not part of the targeted structure. The only galaxy found in the $z = 1.6$ proto-cluster (Noble et al. 2017; R.A. = 03:30:59, decl. = −28:43:06) is actually not detected in the 3 mm continuum map.

ALMA-3 mm.07, ALMA-3 mm.09, ALMA-3 mm.14: These three objects were found in the same project (#2016.1.00754.S), which comprises spectroscopic observations toward multiple submillimeter galaxies selected based on previous 870 μm ALMA continuum imaging. Given the nature of the targeted galaxies (multiple DSFGs), our 3 mm galaxies might be related to the 870 μm selected multiple galaxies, introducing bias and breaking the blindness of our selection. However, here we show that these sources are most likely not related to the main sample and hence they can be considered blind detections. ALMA-3 mm.07 (ALESS75.C in Wardlow et al. 2018), was serendipitously detected in the same field as the 870 μm detected galaxies ALESS75.1 and ALESS75.2 (the original targets of the pointing), which lie at $z_{\mathrm{spec}} = 2.545$ and 2.294, respectively (Danielson et al. 2017). Our source does not show any emission line at the expected frequency of the CO(2−1) line at $z = 2.5$. Unfortunately, the ALMA tunings do not cover the frequencies of the expected CO lines for the $z = 2.29$ solution. Nevertheless, this source shows a very different color ratio from the program's sources ($S_{870\,\mu\mathrm{m}}/S_{3\,\mathrm{mm}} < 17$ versus 114 and >714, respectively), and is even not detected at 870 μm. Actually, Wardlow et al. (2018) reported that this source, ALMA-3 mm.07, has a photometric redshift of $4.00^{+0.07}_{-0.08}$ (Taylor et al. 2009; Cardamone et al. 2010), which is inconsistent with the redshifts of the two original targeted sources. Similarly, ALMA-3 mm.09 (ALESS87.C in Wardlow et al. 2018) shows no emission lines at the searched frequencies and is not detected at 870 μm, contrary to the program's targets (ALESS87.1 and ALESS87.2). Its $S_{870\,\mu\mathrm{m}}/S_{3\,\mathrm{mm}}$ ratio is also very different from the project's sample (<22 versus 28 and >54, respectively) and, as mentioned by Wardlow et al. (2018), is in better agreement with a $z > 4$ galaxy. Finally, ALMA-3 mm.14 is more than 30 arcsec away from the original 870 μm selected objects, and consequently is outside of the ALMA primary beam at that frequency. This source does not show any emission line either, suggesting again a very different redshift solution.

ALMA-3 mm.08, ALMA-3 mm.15, ALMA-3 mm.16: The three sources were detected in different observations of the same project (#2016.1.00171.S), whose targets are galaxies at $z \sim 1.1$. As described in detail in the main text, our galaxies are expected to lie at $z \gtrsim 2.5$, and therefore our detections can be considered unbiased. In fact, ALMA-3 mm.08 has a spectroscopic redshift of $z_{\mathrm{spec}} = 4.55$ (see Table 1), significantly higher than the original sample. Furthermore, ALMA-3 mm.15 and ALMA-3 mm.16 have been found ≳30 arcsec away from the center of the maps, where the main targeted sources are located. This further confirms that those galaxies are not associated with the program's sample.

ALMA-3 mm.12: The project where this source was found targets a sample of starburst galaxies at $z \sim 1.6$ (#2015.1.00861.S), nevertheless, the 3 mm galaxy has a spectroscopic redshift of $z_{\mathrm{spec}} = 2.99$ (see Table 1), indicating that the original sample selection does not introduce any particular bias in our detection.

As has been shown, the 3 mm detected galaxies used in the estimation of the number counts are most likely not related to the original targets of the observations. Actually, most of the original project sources are not detected in the 3 mm continuum images, and the 3 mm selected galaxies show properties very different from the original targeted objects. This confirms the uniqueness of our selection criteria, which likely selects DSFGs at high redshifts. The only possible bias that might be present in our analysis is the gravitational lensing associated with those observations toward clusters of galaxies. Nevertheless, the redshifts of these clusters (z=1.6 and 1.9, respectively) are significantly higher than the typical lens clusters ($z < 1$; e.g., Zavala et al. 2015) and, furthermore, the probability of amplification depends not only on the sources' redshift but also on the angular offset from the cluster position, making the presence of strong lensing unlikely. Besides, these observations only represent ∼6% of the total analyzed area. On the other hand, the amplification by foreground large-scale structures has also been found in blank-field observations (e.g., Aretxaga et al. 2011). All this analysis indicates that our detections are low biased by the original sample selection of the observations and, if any bias is present, it is similar to the one that can plague any other blind survey. Additionally, the maps in which these sources were detected have a large range of depths representative of the whole survey (Figure 6). Finally, we highlight that the rest of the used archival ALMA observations in which no sources were detected show a similar heterogeneous sample

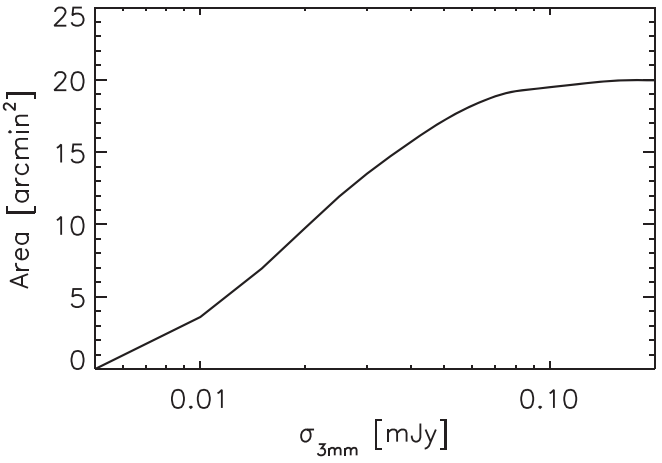

Figure 6. Cumulative area covered by those ALMA maps with blind detections as a function of 1σ rms. As can be seen, the depths probed by these maps encompass a large range from $\sim$6 to 100 μJy.

selection and depths, and therefore, our whole survey is not expected to be significantly biased.

ORCID iDs

J. A. Zavala https://orcid.org/0000-0002-7051-1100
C. M. Casey https://orcid.org/0000-0002-0930-6466
E. da Cunha https://orcid.org/0000-0001-9759-4797
J. Spilker https://orcid.org/0000-0003-3256-5615
J. Staguhn https://orcid.org/0000-0002-8437-0433
J. Hodge https://orcid.org/0000-0001-6586-8845
P. M. Drew https://orcid.org/0000-0003-3627-7485

References

Aravena, M., Decarli, R., Walter, F., et al. 2016, ApJ, 833, 68
Aretxaga, I., Wilson, G. W., Aguilar, E., et al. 2011, MNRAS, 415, 3831
Barger, A. J., Cowie, L. L., Sanders, D. B., et al. 1998, Natur, 394, 248
Béthermin, M., Daddi, E., Magdis, G., et al. 2012, ApJL, 757, L23
Béthermin, M., Wu, H.-Y., Lagache, G., et al. 2017, A&A, 607, A89
Bouwens, R. J., Illingworth, G. D., Oesch, P. A., et al. 2015, ApJ, 803, 34
Brisbin, D., Miettinen, O., Aravena, M., et al. 2017, A&A, 608, A15
Cardamone, C. N., van Dokkum, P. G., Urry, C. M., et al. 2010, ApJS, 189, 270
Carniani, S., Maiolino, R., De Zotti, G., et al. 2015, A&A, 584, A78
Casey, C. M., Hodge, J., Zavala, J. A., et al. 2018a, ApJ, 862, 78
Casey, C. M., Narayanan, D., & Cooray, A. 2014, PhR, 541, 45
Casey, C. M., Zavala, J. A., Spilker, J., et al. 2018b, ApJ, 862, 77
Chabrier, G. 2003, PASP, 115, 763
Cowley, W. I., Lacey, C. G., Baugh, C. M., & Cole, S. 2015, MNRAS, 446, 1784
da Cunha, E., Groves, B., Walter, F., et al. 2013, ApJ, 766, 13
Danielson, A. L. R., Swinbank, A. M., Smail, I., et al. 2017, ApJ, 840, 78
Dunlop, J. S., McLure, R. J., Biggs, A. D., et al. 2017, MNRAS, 466, 861
Ellis, R. S., McLure, R. J., Dunlop, J. S., et al. 2013, ApJL, 763, L7
Finkelstein, S. L. 2016, PASA, 33, e037
Finkelstein, S. L., Ryan, R. E., Jr., Papovich, C., et al. 2015, ApJ, 810, 71
Franco, M., Elbaz, D., Béthermin, M., et al. 2018, A&A, in press, arXiv:1803.00157
Fujimoto, S., Ouchi, M., Ono, Y., et al. 2016, ApJS, 222, 1
Geach, J. E., Dunlop, J. S., Halpern, M., et al. 2017, MNRAS, 465, 1789
Gehrels, N. 1986, ApJ, 303, 336
Hatsukade, B., Kohno, K., Umehata, H., et al. 2016, PASJ, 68, 36
Hatsukade, B., Kohno, K., Yamaguchi, Y., et al. 2018, PASJ, Advance Access
Hatsukade, B., Ohta, K., Seko, A., Yabe, K., & Akiyama, M. 2013, ApJL, 769, L27
Hayward, C. C., Narayanan, D., Kereš, D., et al. 2013, MNRAS, 428, 2529
Hodge, J. A., Karim, A., Smail, I., et al. 2013, ApJ, 768, 91
Hughes, D. H., Serjeant, S., Dunlop, J., et al. 1998, Natur, 394, 241
Ikarashi, S., Caputi, K. I., Ohta, K., et al. 2017, ApJL, 849, L36
Laigle, C., McCracken, H. J., Ilbert, O., et al. 2016, ApJS, 224, 24
Madau, P., & Dickinson, M. 2014, ARA&A, 52, 415
Magdis, G. E., Daddi, E., Béthermin, M., et al. 2012, ApJ, 760, 6
Mantz, A. B., Abdulla, Z., Carlstrom, J. E., et al. 2014, ApJ, 794, 157
McMullin, J. P., Waters, B., Schiebel, D., Young, W., & Golap, K. 2007, ASP Conf. Ser. 376, Astronomical Data Analysis Software and Systems XVI, ed. R. A. Shaw, F. Hill, & D. J. Bell (San Francisco, CA: ASP), 127
Michałowski, M. J., Dunlop, J. S., Koprowski, M. P., et al. 2017, MNRAS, 469, 492
Michałowski, M. J., Watson, D., & Hjorth, J. 2010, ApJ, 712, 942
Molina, J., Ibar, E., Swinbank, A. M., et al. 2017, MNRAS, 466, 892
Noble, A. G., McDonald, M., Muzzin, A., et al. 2017, ApJL, 842, L21
Oesch, P. A., Bouwens, R. J., Illingworth, G. D., et al. 2013, ApJ, 773, 75
Oteo, I., Zwaan, M. A., Ivison, R. J., Smail, I., & Biggs, A. D. 2016, ApJ, 822, 36
Planck Collaboration, Ade, P. A. R., Aghanim, N., et al. 2016, A&A, 594, A13
Riechers, D. A., Bradford, C. M., Clements, D. L., et al. 2013, Natur, 496, 329
Schinnerer, E., Carilli, C. L., Capak, P., et al. 2008, ApJL, 689, L5
Simpson, J. M., Smail, I., Swinbank, A. M., et al. 2015, ApJ, 807, 128
Smail, I., Ivison, R. J., & Blain, A. W. 1997, ApJL, 490, L5
Sobral, D., Smail, I., Best, P. N., et al. 2013, MNRAS, 428, 1128
Staguhn, J. G., Kovács, A., Arendt, R. G., et al. 2014, ApJ, 790, 77
Strandet, M. L., Weiss, A., De Breuck, C., et al. 2017, ApJL, 842, L15
Taylor, E. N., Franx, M., van Dokkum, P. G., et al. 2009, ApJS, 183, 295
Umehata, H., Tamura, Y., Kohno, K., et al. 2015, ApJL, 815, L8
Walter, F., Decarli, R., Aravena, M., et al. 2016, ApJ, 833, 67
Wardlow, J. L., Simpson, J. M., Smail, I., et al. 2018, MNRAS, 479, 3879
Zavala, J. A., Aretxaga, I., Dunlop, J. S., et al. 2018a, MNRAS, 475, 5585
Zavala, J. A., Montaña, A., Hughes, D. H., et al. 2018b, NatAs, 2, 56
Zavala, J. A., Yun, M. S., Aretxaga, I., et al. 2015, MNRAS, 452, 1140